RSC Advances

PAPER

View Article Online
View Journal | View Issue

Cite this: *RSC Adv.*, 2020, **10**, 25125

Selective oxidation of *n*-buthanol to butyraldehyde over $MnCo_2O_4$ spinel oxides

Gheorghita Mitran, *[a] Shaojiang Chen [b] and Dong-Kyun Seo *[b]

Received 29th May 2020
Accepted 25th June 2020

DOI: 10.1039/d0ra04738d

rsc.li/rsc-advances

Partial oxidation of *n*-butanol to butyraldehyde, propionaldehyde and acetaldehyde over $MnCo_2O_4$ spinel oxides has been investigated. Physicochemical characteristics of samples, prepared by co-precipitation with different amounts of precipitating agent, were studied by XRD, N_2 adsorption–desorption isotherms, FT-IR, SEM and XPS. The ratio between the precipitating agent and the precursors has a considerable influence both on the structure, which is evidenced by XRD, due to switching from a crystalline structure to an amorphous one and on the surface (XPS) by an obvious change in the ratio Co^{3+}/Co^{2+} and Mn^{4+}/Mn^{3+} and in the content of oxygen vacancies. The reaction rate is not influenced by the oxygen pressure, emphasizing that *n*-butanol oxidation occurs through the Mars van Krevelen mechanism. The conversion of *n*-butanol and yield of butyraldehyde are directly proportional to the cobalt content on the surface, while the propionaldehyde yield is proportional to the Mn^{4+}/Mn^{3+} ratio.

1 Introduction

There is currently a particular interest for oxidation of higher alcohols (chains of more than 4 carbon atoms), due to their ability to convert relatively easy into valuable products such as aldehydes, esters, ethers and oxygenated fuel additives.[1–3] *n*-Butanol is of special interest being considered a good alternative to gasoline compared to ethanol[4] since it diminishes the energy crisis and reduces hydrocarbon emissions.

The partial oxidation of *n*-butanol to butyraldehyde has been studied to a lesser extent, although it has particular industrial importance due to its use for obtaining many high-value chemicals.[5,6] At the moment, the butyraldehyde production is carried out from propene *via* hydroformylation (oxo-synthesis), but this reaction presents a number of disadvantages such as the thermodynamically favored product is alkane (from hydrogenation of alkene), takes place at high pressures (200 bar), the reaction is homogeneously catalyzed (carbonyl complexes of cobalt or rhodium) and major products are branched aldehyde not linear which are the desired ones.[7,8]

Considering the fact that biobutanol can be produced by the biomass feedstock fermentation, its use as a raw material for the production of butyric aldehydes is very attractive in agreement with the current environmental policies. Withal, many chemical industries are oriented towards the development of environmentally friendly and sustainable processes for selective oxidation of alcohols.[9–11]

The partial oxidation of *n*-butanol, in the gas phase, was studied over Cu and Ru catalysts with good yields to butyraldehyde,[12,13] over Au and Pd supported on titania,[9] over LDH-derived Ni-based catalysts[14] and over platinum supported mesoporous silica CMI-1.[15]

Manganese based catalysts supported on Al_2O_3, CeO_2, ZrO_2, SiO_2 were studied for selective oxidation of 2-butanol to methyl-ethyl-ketone[16] revealing that, the presence of Mn_3O_4 phase is responsible for catalytic activity. Co_3O_4 catalyst has been studied for the total oxidation of *n*-butanol[17] showing that Co^{3+}/Co^{2+} couple represents the active site for the oxidation reactions by a redox mechanism.

After our knowledge, spinel type $MnCo_2O_4$ oxides have not so far been studied in the partial oxidation of *n*-butanol. Among other spinel oxides, those of cobalt–manganese are particularly interesting because they contain metals with more than one oxidation state, which could be placed in any of the two sites (tetrahedral or octahedral), modifying the structural and respectively chemical properties. The difficulty for this type of oxides is represented by the identification of the oxidation state and the cations distribution in tetrahedral or octahedral sites.[18] The cobalt and manganese cations in superior oxidation states, Co^{3+}, Mn^{3+} and Mn^{4+} are usually placed in octahedral positions, while the cations in inferior oxidation state (Co^{2+}, Mn^{2+}) have no preference.

Herein, we have evaluated the behavior of cobalt-manganese spinel oxides, prepared by coprecipitation using different molar ratio between the precipitation agent and Co + Mn, in selective oxidation of *n*-butanol to butyraldehyde.

[a]*Laboratory of Chemical Technology and Catalysis, Department of Organic Chemistry, Biochemistry & Catalysis, University of Bucharest, 4-12, Blv. Regina Elisabeta, 030018 Bucharest, Romania. E-mail: geta_mitran@yahoo.com; geta.mitran@chimie.unibuc.ro*

[b]*School of Molecular Sciences, Arizona State University, Tempe, AZ, 85287-1604, USA. E-mail: DSeo@asu.edu*

2 Experimental

2.1. Catalysts preparation

The spinel type oxides based on cobalt and manganese, with formula $MnCo_2O_4$ were prepared by co-precipitation method. For this purpose, the mixture of $(CH_3COO)_2Co\cdot 4H_2O$ (99.99% from Merck) and $(CH_3COO)_2Mn\cdot 4H_2O$ (99.99% from Merck) solutions in water has been homogenized by stirring for 30 min. Ammonium carbonate (99.99% from Merck), dissolved in water, was chosen as a precipitating agent, with different (Co + Mn)/NH_4^+ molar ratios (1 : 2, 1 : 3, 1 : 4), denoted $MnCo_2O_4$(2), $MnCo_2O_4$(3) and respectively $MnCo_2O_4$(4). The precipitating agent was added dropwise, with continuous stirring, over the precursor solution. The obtained precipitates were separated through centrifugation, washed for more times with distilled water, dried at 60 °C for 24 h and calcined at 500 °C (5 °C min^{-1}) for 6 h.

2.2. Catalysts characterization

The samples structure was analyzed with a PANalyticalX'Pert Pro MRD X-ray diffractometer with a Cu K_α radiation ($\lambda = 0.1514$ nm). Data were recorded in the 2θ range of 5–80° with a step size of 0.0251°. The specific surface area (determined by the Brunauer–Emmett–Teller (BET) methods, in the relative pressure region P/P_0 0.06–0.2) and the porosity measurements (calculated by Barrett–Joyner–Halenda (BJH) method) were performed from the nitrogen adsorption–desorption isotherms, using a Micromeritics ASAP 2020. Scanning electron microscope (SEM) morphology and the energy dispersive X-ray (EDX) composition of the samples were

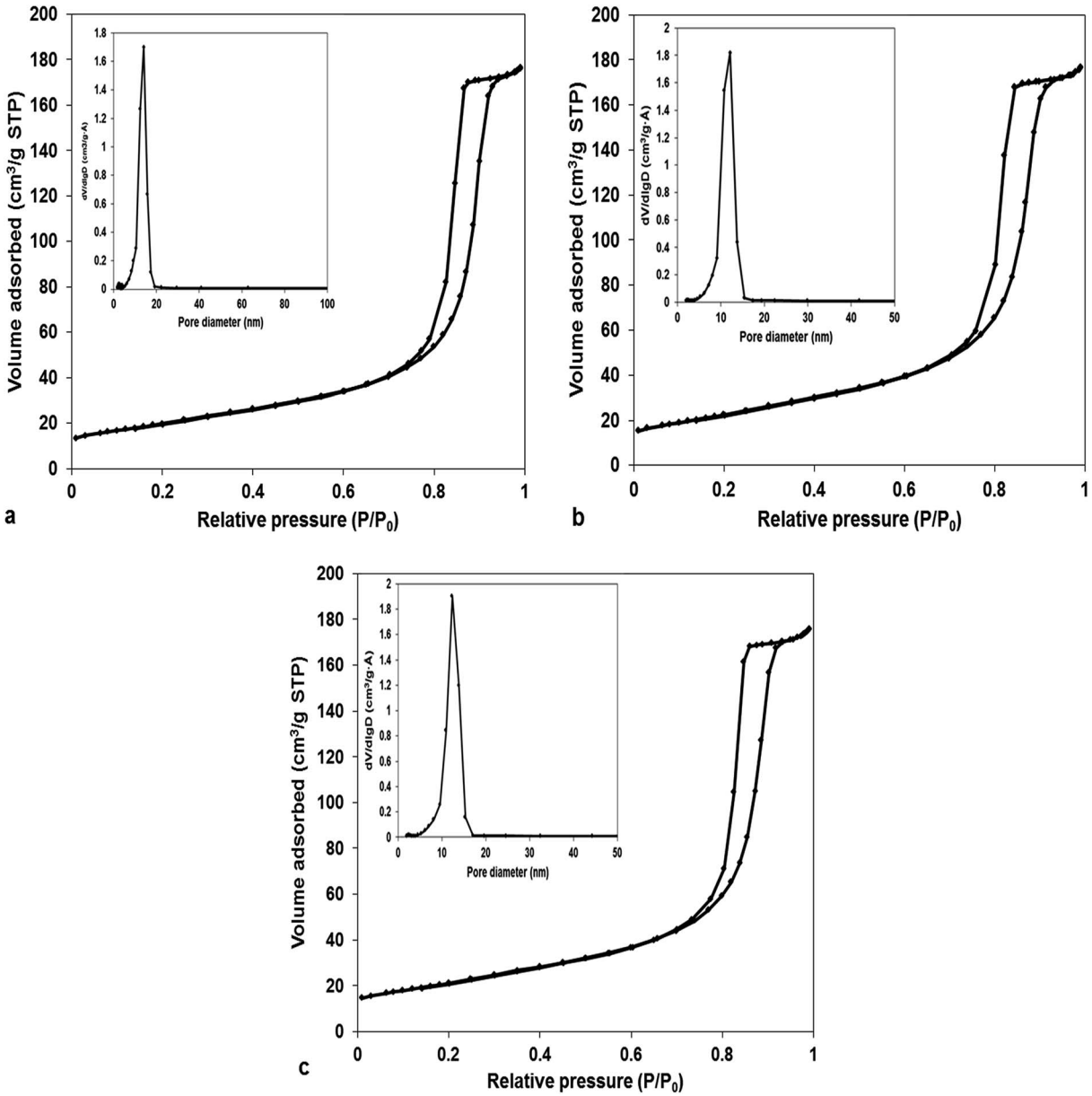

Fig. 1 N_2 adsorption–desorption isotherm and pore size distribution of $MnCo_2O_4$ samples: (a) $MnCo_2O_4$(2); (b) $MnCo_2O_4$(3); (c) $MnCo_2O_4$(4).

collected on a XL-30 Environmental SEM. X-ray photoelectron spectra (XPS) were collected on a VG-220IXL spectrometer equipped with a monochromated Al Kα radiation (1486.6 eV, line width 0.8 eV), and the energy resolution of 0.4 eV. The C1s peak (284.8 eV) was used as a reference. Deconvolution of spectra was recorded with CASAXPS software, using the Shirley background. Information on metal oxygen linkages was obtained by Fourier transform infrared (FT-IR) with a Bruker IFS 66 V/S spectrometer, equipped with a diamond attenuated total reflectance (ATR), with a resolution of 4 cm^{-1}, covering a spectral range of 400–4000 cm^{-1}.

2.3. Catalytic activity test

The partial oxidation of *n*-butanol has been carried out in a continuous-flow fixed bed reactor (8 mm i.d.) at atmospheric pressure. The reaction temperature, monitored by electronic control, was varied in the range 100–250 °C. The mixture of reaction has been achieved by passing air through a stainless steel saturator with *n*-butanol, enabling an *n*-butanol concentration of 400 ppmv in air. The saturated vapor pressure of butanol was determined from Antoine equation and used for calculation of ppmv concentration. The amount of catalyst used was 0.2 g. The space velocity, expressed as $F_{reactants}/W_{cat}$, was varied between 9000 and 21 000 mL g^{-1} h^{-1}.

The analysis of reactants mixture and the reaction products (after a stabilization time of 30 min) was performed with a GC K072320 Thermo-Quest gas chromatograph equipped with an FID detector. The *n*-butanol conversion and the products yields were determined from three successive measurements with formulas:

$$SD = \sqrt{\frac{\sum_{i=1}^{n}(x_i - \bar{x})^2}{n}}$$

$$\bar{x} = \frac{1}{n}\sum_{i=1}^{n} x_i$$

where SD – standard deviation, n – number of measurements, $\bar{x}$ – the mean of x_i

3 Results and discussion

3.1. Characterization of catalysts

In order to investigate the specific surface areas and pore-size distribution of $MnCo_2O_4$ catalysts, Brunauer–Emmett–Teller (BET) gas-sorption measurements were performed. N_2 adsorption–desorption isotherms at 77 K are presented in Fig. 1. Likewise, the specific surface area, pore volume and average pore diameter are shown in Table 1. The isotherms could be classified as type IV with a type H1 hysteresis loop, characteristic for mesoporous structure. The average pore diameter, from BJH desorption, is about 14.0 nm for sample 1, and respectively 12.1 nm for samples 2 and 3, confirming that all the samples contain mesoscale pores. Also, the size distribution is very narrow the majority of pores are in the range 9–15 nm. The (Co + Mn)/NH_4^+ molar ratios did not affect the volume of mesoporous, keeping it at 0.27 cm^3 g^{-1} irrespective of the amount of ammonium used. Conversely, the specific surface area increases at ammonium amount increasing from 71 to 86 m^2 g^{-1}.

Table 1 Textural properties of Co–Mn mixed oxides

Sample	S_{BET} (m^2 g^{-1})	V_{micro} (cm^3 g^{-1})	V_{meso} (cm^3 g^{-1})	d_{meso}[a] (nm)
$MnCo_2O_4$(2)	71	0.0001	0.27	14.1
$MnCo_2O_4$(3)	81	0.0001	0.27	12.1
$MnCo_2O_4$(4)	86	0.0002	0.27	12.1

[a] BJH desorption average pore diameter.

Diffraction patterns of samples are shown in Fig. 2. The diffraction peaks of the first two catalysts correspond to mesoporous $MnCo_2O_4$ spinel oxide phases (Card PDF 01-084-0482) and show better crystallinity than the third catalyst. The purity of all prepared samples was evidenced by the absence of other peaks than those corresponding to $MnCo_2O_4$ spinel. The cell parameter "*a*" increases from 8.11 Å for $MnCo_2O_4$(2), to 8.12 Å for $MnCo_2O_4$(3) and respectively 8.16 Å for $MnCo_2O_4$(4) catalyst. The cell parameter "*a*" has been determined from line corresponding to $2\theta = 42.5°$ and Miller indices (*hkl*-311). The standard deviation for cell parameters is ±0.005 Å. A peak broadening has been highlighted for the (311) plane of all samples. Usually, a peak broadening is correlated with the decreasing of crystallite size and stress/strains induced in the nanoparticles.[19] The average crystallite size (d) was calculated with the Scherrer formula:

$$d = 0.9\lambda/\beta \cos\theta$$

where λ is the X-ray wavelength, β is the full-width at half maximum (FWHM), and θ is the diffraction angle. The average crystallite size, calculated for $2\theta = 36$, 43 and 52°, has been

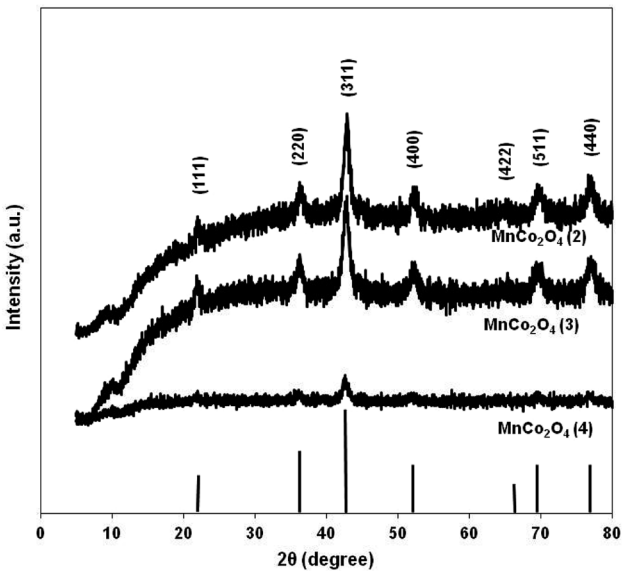

Fig. 2 XRD patterns of $MnCo_2O_4$ spinel oxides.

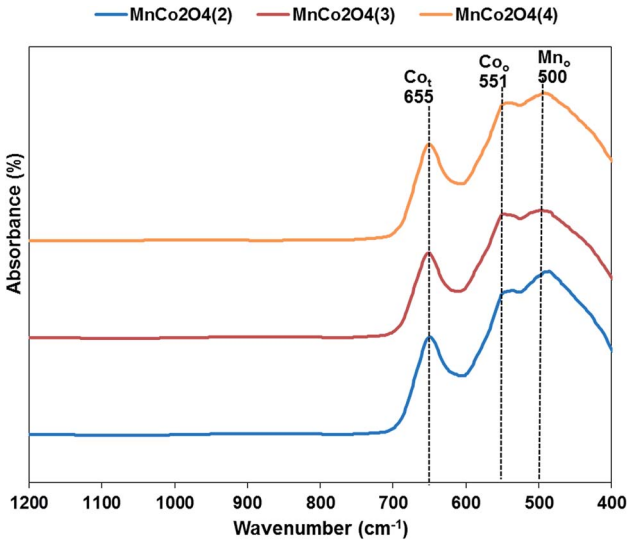

Fig. 3 FT-IR spectra of $MnCo_2O_4$ nanoparticles synthesized by coprecipitation with different (Co + Mn)/NH_4^+ molar ratios (1 : 2, 1 : 3, 1 : 4).

estimated at 20.4 nm for $MnCo_2O_4$(2), 19.2 nm for $MnCo_2O_4$(3) and 7 nm for $MnCo_2O_4$(4).

The FT-IR spectra for all samples are shown in Fig. 3. Three distinctive bands are observed in the spectrum, at 655 cm^{-1} corresponding to the stretching vibration of Co^{2+}–O bond located in tetrahedral units of the spinel structure, at 551 cm^{-1} corresponding to octahedral units of Co^{3+}–O and at 500 cm^{-1} which corresponds of Mn^{3+}(Mn^{4+})–O from the octahedral positions of the spinel.[20] The peaks corresponding to octahedral positions are shifted towards higher wavenumber from first to third catalyst, emphasizing that the interactions between Co and Mn are different in the three samples.

The bulk composition of $MnCo_2O_4$ nanoparticles was determined by EDX analysis and is shown in Table 2 and Fig. 4, and has been observed that Co, Mn and O are the main detected elements. The atomic compositions determined by EDX emphasize that the ratio between Co and Mn is very closed to 2, while the ratio between O and Co and between O and Mn is lower than the one calculated (2) suggesting the existence of oxygen vacancies in the prepared samples.

The morphology of synthesized $MnCo_2O_4$ samples (Fig. 5) investigated by SEM evidenced the presence of microspheres that are formed by the aggregation of nanoparticles, with a hierarchical structure well-defined and well-dispersed like a flower.

The identification of the chemical states and the composition of species on the surface were carried out using XPS spectra of all samples that are shown in Fig. 6. The peak of C 1s, which is used as standard, was evidenced at 284.8 eV. The Co $2p_{3/2}$ spectra confirm the presence of Co^{2+} and Co^{3+} on the surface. The binding energies of Co^{2+} species are located in the region 780.6–781.5 eV, the value of binding energy decreasing continuously from the first to the third catalyst. The Co^{3+} species present peaks in the region 778.8–780 eV, the binding energy decreasing in the same order, which indicates a decrease in the interaction between Co and Mn in the same order. The satellite peak at 784.6–785.3 eV is ascribed to Co^{2+} in tetrahedral oxygen coordination while the satellite peak from 789.1 eV is characteristic of Co^{3+} species in octahedral coordination, according to literature data.[21]

Table 2 The EDX composition of $MnCo_2O_4$ spinel oxides

	Wt (%)			At (%)					
Catalyst	Co	Mn	O	Co	Mn	O	Co/Mn	O/Co	O/Mn
$MnCo_2O_4$(2)	53.69	23.9	22.41	33.17	15.84	50.99	2.09	1.53	3.2
$MnCo_2O_4$(3)	52.21	23.58	24.21	31.32	15.18	53.50	2.06	1.70	3.5
$MnCo_2O_4$(4)	55.72	23.95	20.32	35.66	16.44	47.90	2.16	1.34	2.9

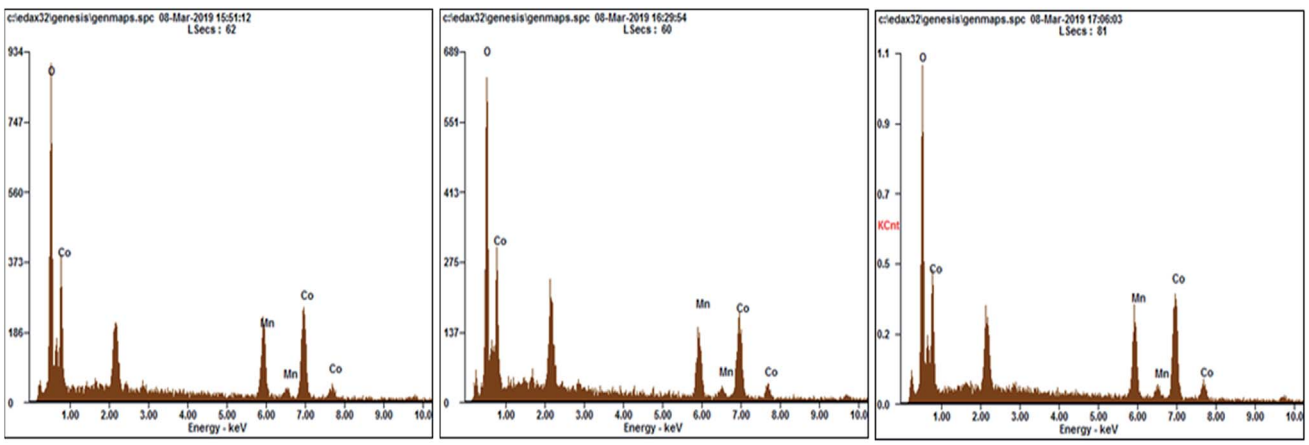

Fig. 4 EDX analysis of the $MnCo_2O_4$ spinel oxides.

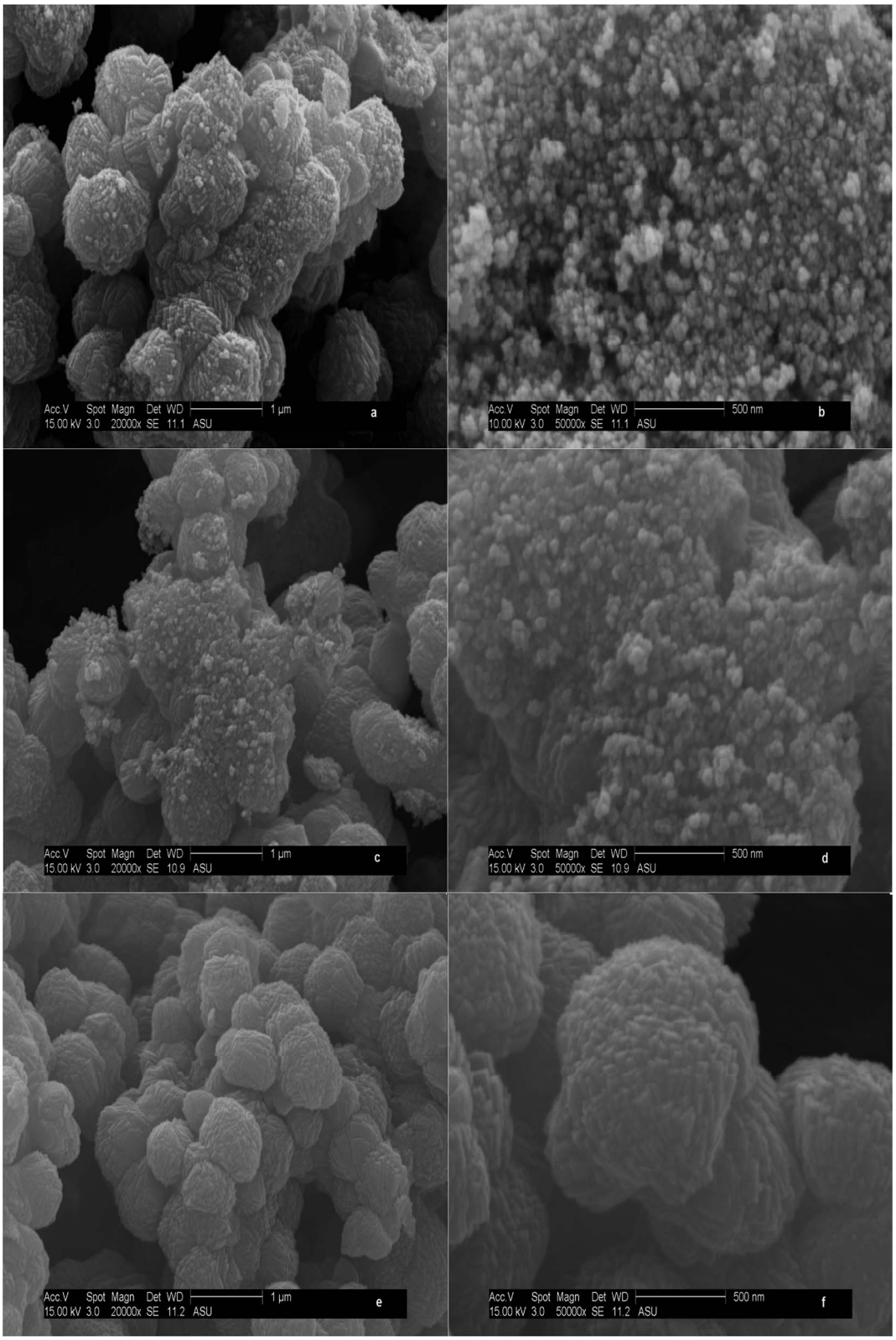

Fig. 5 SEM images of $MnCo_2O_4$ spinel oxides: (a and b) $MnCo_2O_4$(2), (c and d) $MnCo_2O_4$(3), (e and f) $MnCo_2O_4$(4).

The ratio between Co^{3+}/Co^{2+} also decreases from first to last catalyst (Table 3) from 1.53 to 1.41 and respectively to 0.73. The species of cobalt with lower valence do not contribute to oxygen vacancies formation, therefore it is expected that by increasing of Co^{3+} composition to increase the percentage of oxygen vacancies by the process: $2Co^{3+} + O^{2-} \rightarrow 2Co^{2+} + \square + 1/2O_2$.

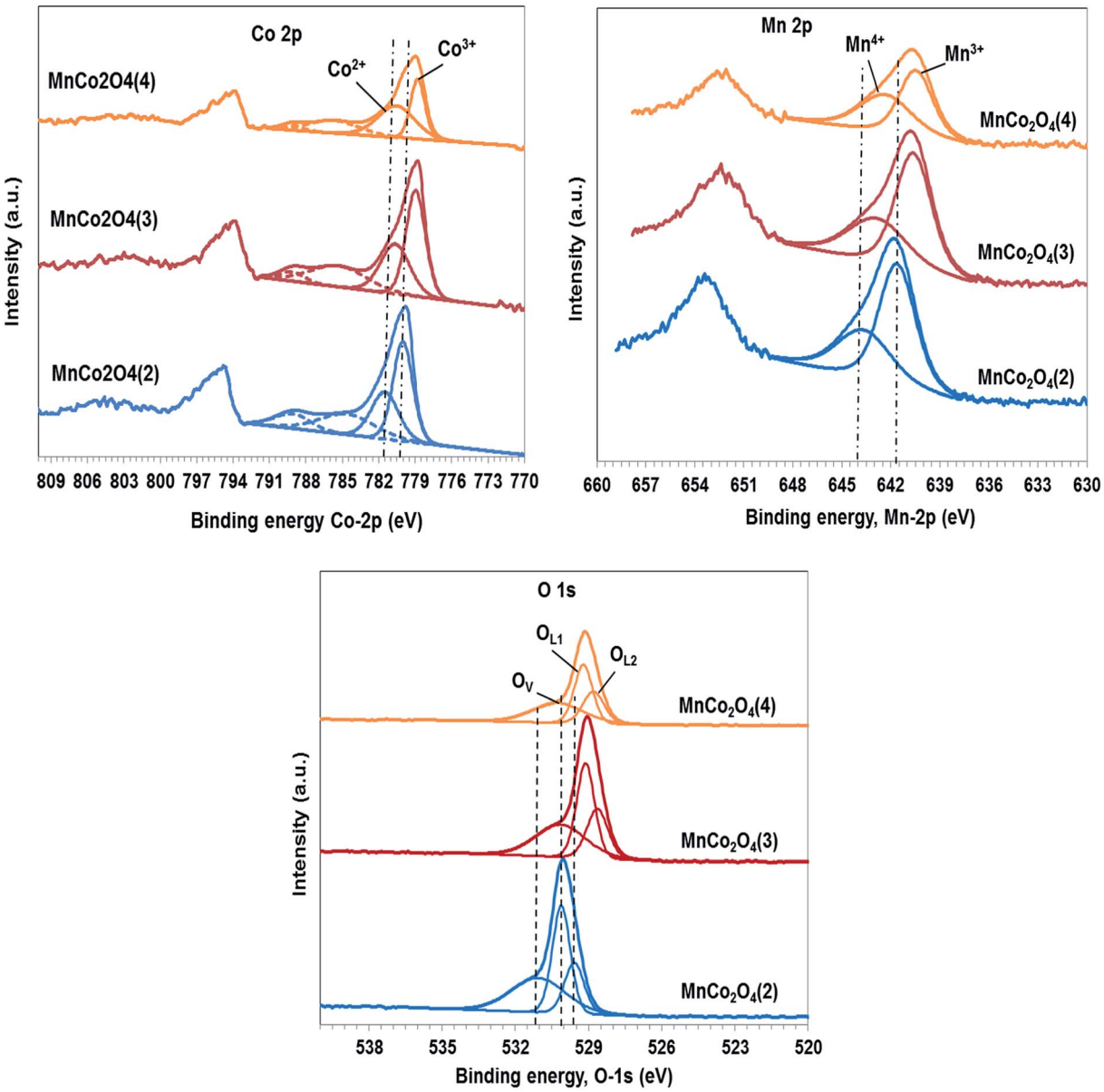

Fig. 6 XPS spectra of $MnCo_2O_4$ spinel oxides with different ratios (Co + Mn)/NH_4^+.

Table 3 The elemental surface composition from XPS

	At[a] (%)								Co/Mn
Catalyst	Co	Mn	O	Co^{3+}/Co^{2+}	Mn^{4+}/Mn^{3+}	O_{L1} (%)	O_{L2} (%)	O_V (%)	XPS
$MnCo_2O_4(2)$	26.7	12.7	48.7	1.53	0.59	40.09	20.82	39.08	2.09
$MnCo_2O_4(3)$	26.2	17.4	47.8	1.41	0.61	38.99	23.76	37.26	1.51
$MnCo_2O_4(4)$	24.5	17.0	49	0.73	0.83	38.60	24.53	36.87	1.44

[a] The difference is represented by C percent.

The spectra of Mn $2p_{3/2}$ confirm the presence of Mn^{3+} and Mn^{4+} as the major manganese species. The peak corresponding to Mn^{3+} is located at 640.5–641.6 eV[22] the binding energy values decreasing at NH_4^+/(Co + Mn) molar ratio in the catalysts preparation increasing. The peak at 642.3–643.6 eV corresponds to Mn^{4+} cations being shifted in the same order as that of Mn^{3+}

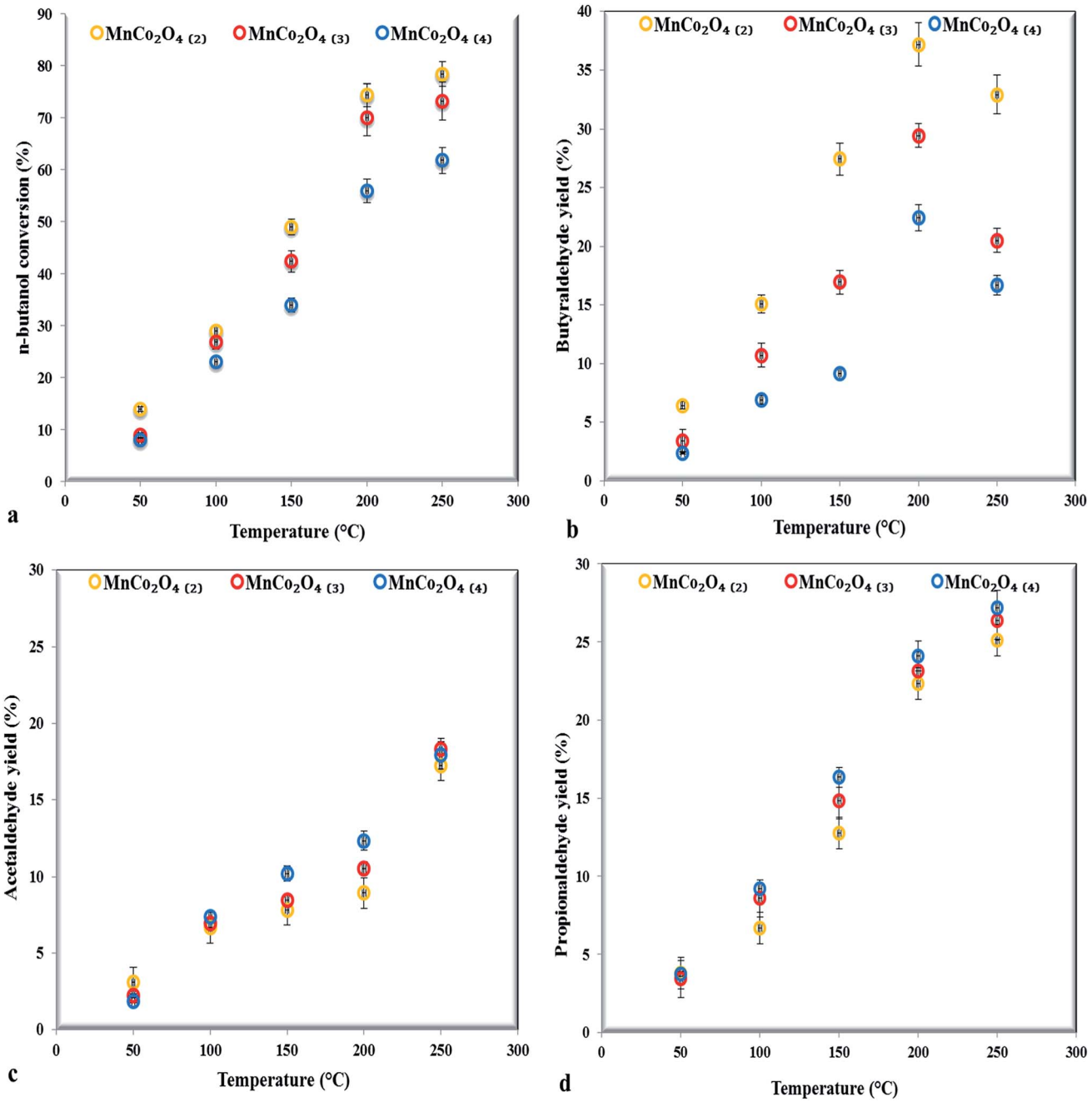

Fig. 7 The catalytic performance of $MnCo_2O_4$ samples for *n*-butanol selective oxidation (a), butyraldehyde (b), acetaldehyde (c) and propionaldehyde (d) yield (0.2 g catalyst, 400 ppmv *n*-butanol).

cations. The ratio between Mn^{4+}/Mn^{3+} increases in order $MnCo_2O_4(2)$ (0.59) < $MnCo_2O_4(3)$ (0.61) < $MnCo_2O_4(4)$ (0.83), in the same way should increase the percentage of oxygen vacancies. The ratio Co/Mn on the surface is 2 for the first sample while for the second and the third sample is approximately 1.5.

The O 1s peaks are fitted at 528.6–530.1 eV, typical for lattice oxygen in the metal–oxygen bond[23] which is split into two peaks, one corresponding to oxygen lattice of cobalt oxide (O_{L1}), and the other to oxygen lattice of manganese oxide (O_{L2}); while the peak situated at 530.2–531.0 eV is associated with oxygen defects in the subsurface. Percentage of lattice oxygen corresponding to cobalt oxide decrease at Co/Mn ratio decreasing, while the percentage of lattice oxygen corresponding to manganese oxide increase at manganese composition on the surface increasing. The composition of oxygen defects, on the surface of the first sample, is with approximately 2–2.5% more than for the others. Presence of oxygen vacancies can promote Co^{3+} and respectively Mn^{4+} formation that contribute to active oxygen species apparition like peroxo (O_2^{2-}) or superoxo (O_2^-) on the catalyst surface. The standard deviation for composition of oxygen defects has been of ±5%.

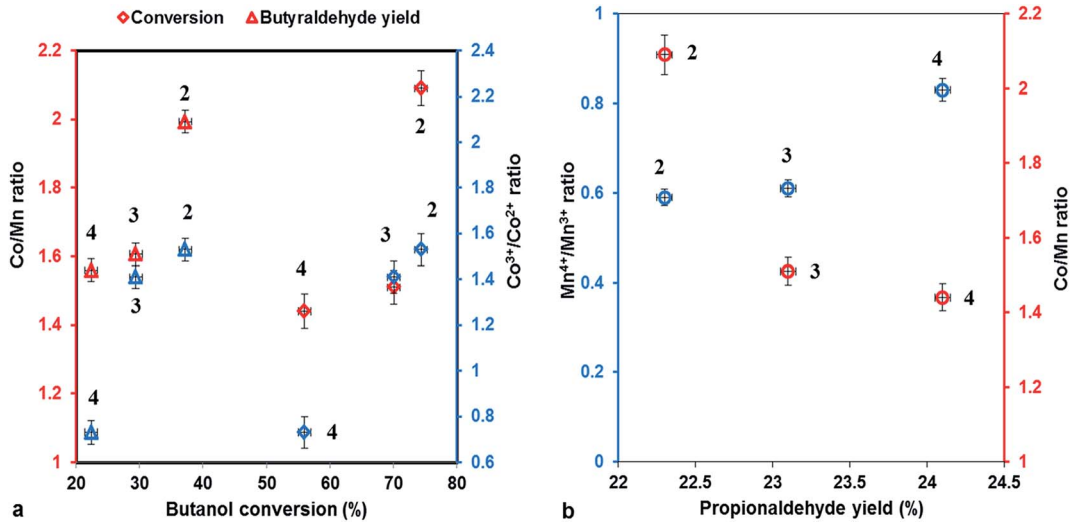

Fig. 8 The butanol conversion and butyraldehyde yield as function of Co/Mn and respectively Co^{3+}/Co^{2+} ratio (a) and propionaldehyde yield as function of Mn^{4+}/Mn^{3+} ratio and respectively Co/Mn ratio (b) (0.2 g catalyst, 400 ppmv *n*-butanol, 200 °C).

3.2. Catalytic activity

The partial oxidation of *n*-butanol, in the gas phase, was studied over $MnCo_2O_4$ catalysts. The *n*-butanol conversion and the products yields as a function of reaction temperature, for three successive measurements, over all studied catalysts are shown in Fig. 7. The experimental errors are up to ±5%, as shown in error bars from graphs. The conversion increased with temperature increasing for all catalysts. The catalyst with ratio (Co + Mn)/NH_4^+ equal with 2 showed a higher conversion compared to others, in the case of the other two catalysts the conversion decreases with increasing of the ammonium content. The T_{50} temperature (50% *n*-butanol conversion) is at 120 °C, for the first catalyst, at 148 °C and respectively 165 °C for the second and third catalyst. The activity was improved by the presence of spinel structure as could be observed from XRD patterns.

The major products observed are butyraldehyde, propionaldehyde and acetaldehyde while formaldehyde was detected in traces. The *n*-butyraldehyde yields increased with temperature increasing, reaching a maximum at 200 °C then decreasing, probably due to the secondary combustion reactions of butyraldehyde, as observed by Jiang[24] in partial oxidation reaction of butanol to butyraldehyde over a series of perovskites with Mn, Fe and Co. The highest yield in butyraldehyde (37%) was

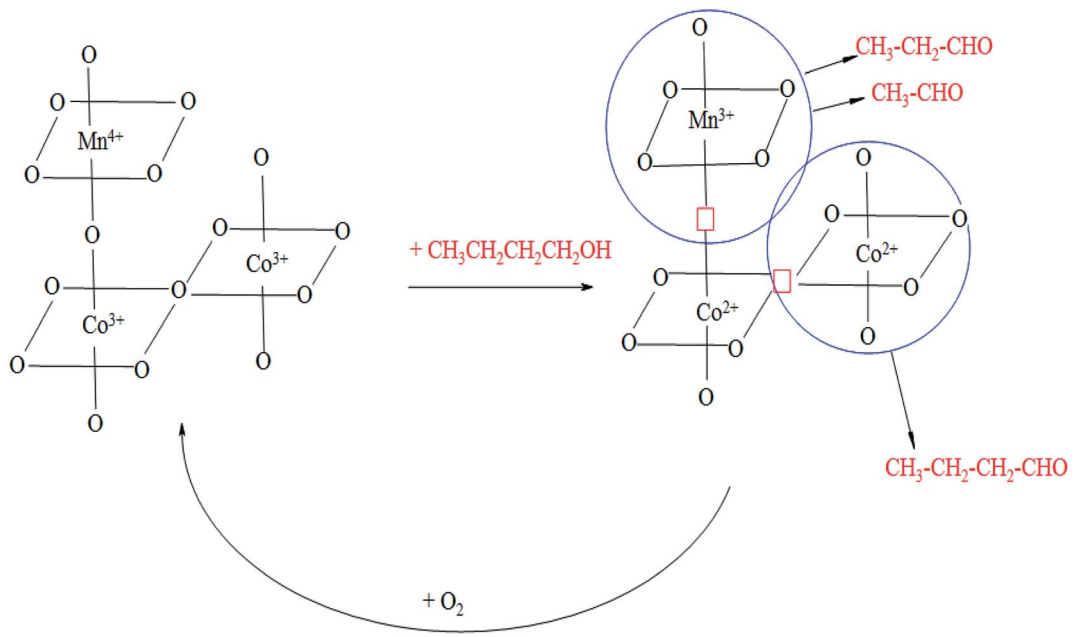

Scheme 1 Selective oxidation of *n*-butanol over $MnCo_2O_4$ spinel.

achieved on the first samples with higher ratio Co/Mn and Co^{3+}/Co^{2+} (from XPS). Our results are in agreement with those reported by Xie[25] in carbon monoxide oxidation observing that Co^{3+} represents the active site for reaction, while the Co^{2+} was almost inactive.

The propionaldehyde and acetaldehyde yields, conversely, increased with temperature increasing, in line with the increase of Mn^{4+}/Mn^{3+} ratio, proving that manganese is more effective for breaking of C–C bonds than cobalt. The presence in octahedral positions of both cobalt and manganese trivalent and tetravalent cations leads to appearance of active sites, octahedral positions being more reactive than tetrahedral ones towards the oxidation reactions that occur by Mars–van-Krevelen mechanism.[26]

The correlation between conversion of butanol, yield of butanal, respectively propanal and Co/Mn, Co^{3+}/Co^{2+}, Mn^{4+}/Mn^{3+} ratios is shown in Fig. 8, emphasizing that the conversion and the butanal yield depend of Co/Mn ratio and Co^{3+}/Co^{2+} ratio, being directly proportional to them, while the propanal yield increase to Mn loading and Mn^{4+}/Mn^{3+} ratio increasing.

Based on these findings we propose the following scheme of oxidation of *n*-butanol on the studied catalysts (Scheme 1).

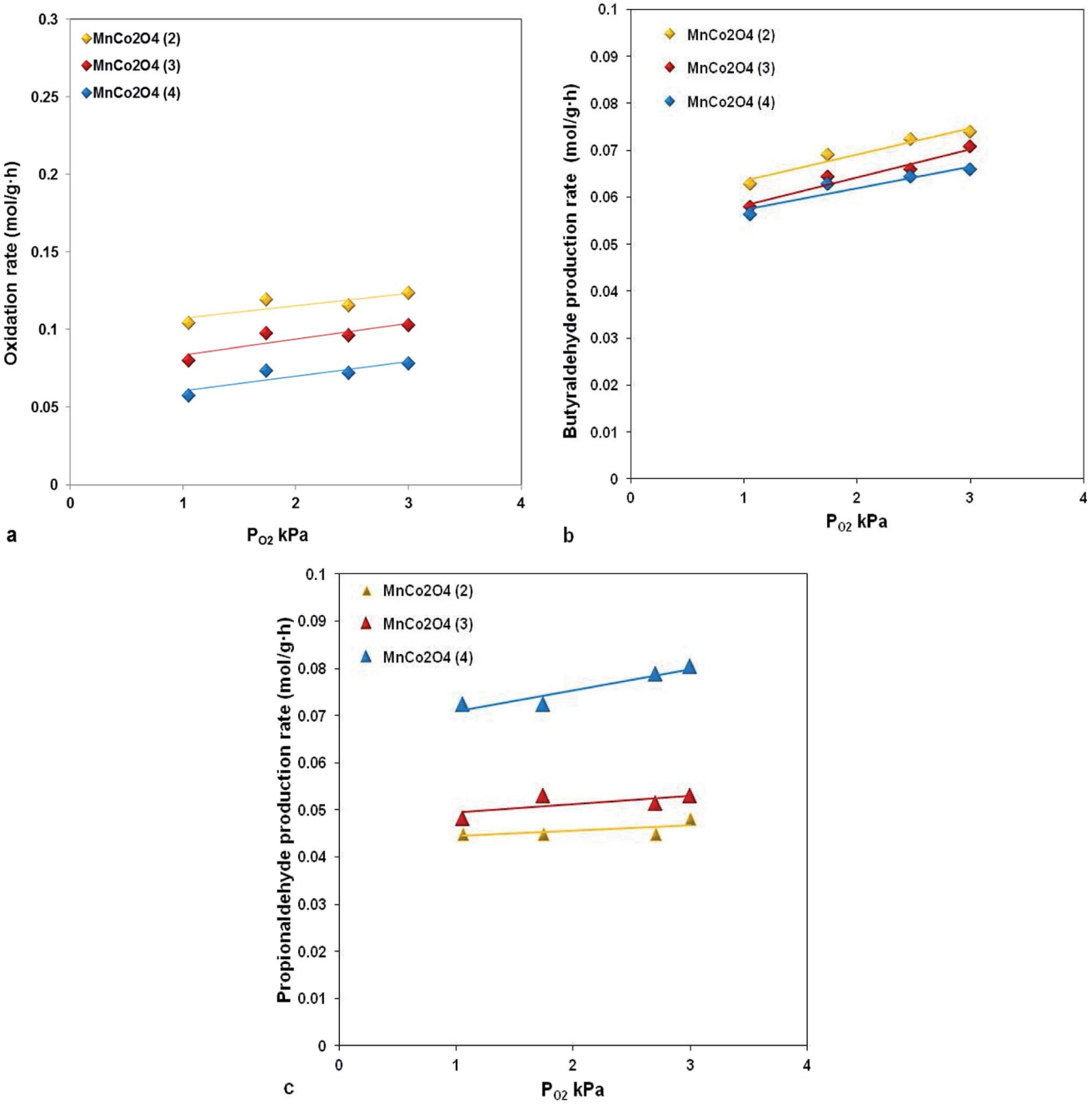

Fig. 9 The reaction rate dependence on oxygen partial pressure.

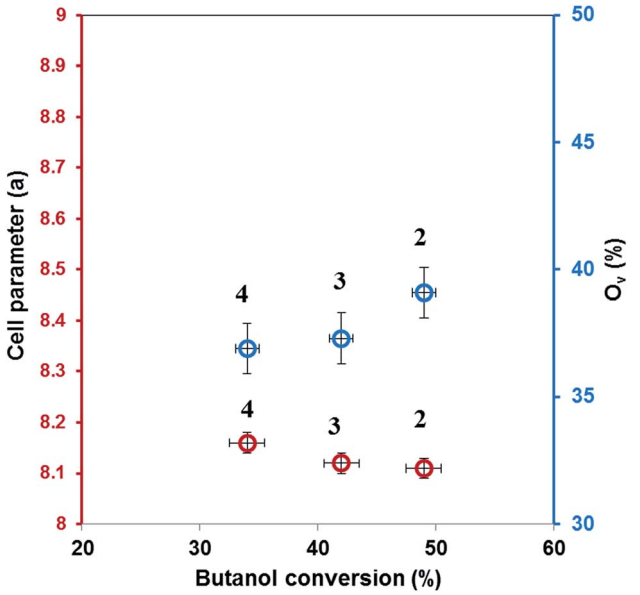

Fig. 10 Cell parameter and oxygen defects influence on butanol conversion.

The reaction rate dependence as function of oxygen partial pressure, presented in Fig. 9, evidenced that an increasing in oxygen partial pressure almost does not have any influence on the reaction rate both in terms of reactants and reaction products. This type of behavior is specific to the reactions which occur through the Mars van Krevelen mechanism, where the lattice oxygen is implied in oxidation reaction.

For our catalysts the presence of oxygen vacancies which ensure the mobility of lattice oxygen is evidenced from XRD by decreasing of lattice parameter and from XPS, the catalyst with lowest parameter and with highest concentration of active oxygen species, $MnCo_2O_4$(2), has the highest activity (Fig. 10).

4 Conclusions

Partial oxidation of *n*-butanol over cobalt–manganese spinel oxides, prepared by coprecipitation with different amounts of ammonium carbonate, has been examined. The active sites for this reaction are represented by the Co^{3+} cations and Mn^{3+}/Mn^{4+} cations, situated in octahedral positions, these being more reactive than tetrahedral position towards the oxidation reactions, that occur by Mars–van-Krevelen mechanism.

The *n*-butanol conversion and the yield to butyraldehyde are directly proportional to Co/Mn ratio and Co^{3+}/Co^{2+} ratio, while the propionaldehyde yield increase to Mn loading and to Mn^{4+}/Mn^{3+} ratio increasing.

The oxygen vacancies presence ensures lattice oxygen mobility, contributing to increasing the concentration of active oxygen species and respectively to increase the catalytic activity.

Conflicts of interest

There are no conflicts to declare.

References

1 R. B. Wagh and J. M. Nagarkar, *Tetrahedron Lett.*, 2018, **59**, 3443–3447.
2 M. Amini, M. Mahdi Najafpour, M. Zare and E. Amini, *J. Mol. Catal. A: Chem.*, 2014, **394**, 303–308.
3 F. Saberi, D. Rodríguez-Padrón, E. Doustkhah, S. Ostovar, A. Franco, H. Reza Shaterian and R. Luque, *Catal. Commun.*, 2019, **118**, 65–69.
4 M. Franco Finol, J. Rooke, S. Siffert, R. Cousin, P. Carniti, A. Gervasini, J.-M. Giraudon, B.-L. Su and J.-F. Lamonier, *New J. Chem.*, 2014, **38**, 1988–1995.
5 A. Mahajan, S. Banik, D. Majumdar and S. K. Bhattacharya, *ACS Omega*, 2019, **4**, 4658–4670.
6 I. Gandarias, E. Nowicka, B. J. May, S. Alghareed, R. D. Armstrong, P. J. Miedziak and S. H. Taylor, *Catal. Sci. Technol.*, 2016, **6**, 4201–4209.
7 A. Haynes, P. M. Maitlis, G. E. Morris, G. J. Sunley, H. Adams, P. W. Badger, C. M. Bowers, D. B. Cook, P. I. Elliott, T. Ghaffar, H. Green, T. R. Griffin, M. Payne, J. M. Pearson, M. J. Taylor, P. W. Vickers and R. J. Watt, *J. Am. Chem. Soc.*, 2004, **126**, 2847–2861.
8 H. Bahrmann, H. Bach, *Ullmann'S Encyclopedia of Industrial Chemistry: Oxo Synthesis*, Wiley-VCH Verlag GmbH & Co. KGaA, 7th ed, 2005.
9 Y. Khan, M. Marin, T. Viinikainen, J. Lehtonen, R. L. Puurunen and R. Karinen, *Appl. Catal., A*, 2018, **562**, 173–183.
10 W. Huang, B. Chiyin Ma, H. Lu, R. Li, L. Wang, K. Landfester and K. A. I. Zhang, *ACS Catal.*, 2017, **78**, 5438–5442.
11 H. B. Ji, K. Ebitani, T. Mizugaki and K. Kaneda, *Catal. Commun.*, 2002, **3**(11), 511–517.
12 J. Requies, M. B. Güemez, A. Iriondo, V. L. Barrio, J. F. Cambra and P. L. Arias, *Catal. Lett.*, 2012, **142**, 417–426.
13 J. Requies, M. B. Güemez, P. Maireles, A. Iriondo, V. L. Barrio, J. F. Cambra and P. L. Arias, *Appl. Catal., A*, 2012, **423–424**, 185–191.
14 L. Huang, J. Zhou, A. T. Hsu and R. Chen, *Int. J. Hydrogen Energy*, 2013, **38**, 14550–14558.
15 S. Sabour, C. Especel, C. Fontaine, M. Bidaoui, L. Benatallah, N. Saib-Bouchenafa, J. Barbier Jr and O. Mohammedi, *J. Mol. Catal. A: Chem.*, 2016, **420**, 50–55.
16 K. Prabu, M. Prabu, A. K. Venugopal, A. T. Venugopalan, W. V. Y. S. Sandilya, C. S. Gopinath and T. Raja, *Appl. Catal., A*, 2016, **525**, 237–246.
17 P. Mountapmbeme Kouotou and Z. Y. Tian, *Surf. Coat. Technol.*, 2017, **326**, 11–17.
18 A. N. Naveen and S. Selladurai, *Physica B*, 2015, **457**, 251–262.
19 R. Tholkappiyan, A. Nirmalesh Naveen, S. Sumithra and K. Vishista, *J. Mater. Sci.*, 2015, **50**(17), 5833–5843.
20 K. Cheng, F. Yang, G. Wang, J. Yin and D. Cao, *J. Mater. Chem. A*, 2013, **1**, 1669–1676.
21 L. Daheron, R. Dedryvere, H. Martinez, M. Menetrier, C. Denage, C. Delmas and D. Gonbeau, *Chem. Mater.*, 2008, **20**, 583–590.

22 J. M. Cerrato, M. F. Hochella Jr, W. R. Knocke, A. M. Dietrich and T. F. Cromer, *Environ. Sci. Technol.*, 2010, **441**, 55881–55886.
23 J. F. Marco, J. R. Gancedo, M. Gracia, J. L. Gautier and F. J. Berry, *J. Solid State Chem.*, 2000, **153**, 74–81.
24 B. S. Jiang, R. Chang, Y. C. Hou and Y. C. Lin, *Ind. Eng. Chem. Res.*, 2012, **51**, 13993–13998.
25 X. Xie, Y. Li, Z. Q. Liu, M. Haruta and W. Shen, *Nature*, 2009, **458**, 746–749.
26 A. Choya, B. Rivas, J. I. Gutiérrez-Ortiz and R. López-Fonseca, *Catalysts*, 2018, **8**, 427.